Journal of Asian Earth Sciences 124 (2016) 269–283

Contents lists available at ScienceDirect

Journal of Asian Earth Sciences

journal homepage: www.elsevier.com/locate/jseaes

Full length article

# A coupled remote sensing and the Surface Energy Balance based algorithms to estimate actual evapotranspiration over the western and southern regions of Saudi Arabia

Shereif H. Mahmoud *, A.A. Alazba

*Alamoudi Water Research Chair, King Saud University, PO Box: 2460, Riyadh 11451, Saudi Arabia*

ARTICLE INFO

*Article history:*
Received 15 February 2016
Received in revised form 4 May 2016
Accepted 9 May 2016
Available online 9 May 2016

*Keywords:*
Actual evapotranspiration (AET)
SEBAL
Irrigated cropland
Water consumption
Saudi Arabia

ABSTRACT

In countries with absolute water scarcity such as the Kingdom of Saudi Arabia (KSA), large-scale actual evapotranspiration estimation is of great concern in water use practices. Herein, spatial and temporal distribution of actual evapotranspiration (AET) in the western and southern regions of KSA during 1992–2014 was estimated using the SEBAL model with field observations. Zonal statistics for each land use-cover type were also identified, in order to understand their effects on water consumption. In addition, daily and seasonal water consumption for major crops was computed. Results revealed a gradual increase in monthly AET values from January to April and subsequent decline from May to December. The maximum monthly AET values were observed for irrigated cropland in southwestern, central, and southeastern regions of Asir Province, central and southwestern regions of Al-Baha Province, central and the plains region of Jazan Province, southern portion of Makkah Province, and limited areas in the northern regions of Madinah Province. The annual AET ranged from 418.8 to 3442.3 mm $yr^{-1}$. The normal distribution of mean annual AET values ranged from 717 to 1020 mm $yr^{-1}$. Forty-two percent of the study area had an annual AET that ranged from 717 to 1020 mm $yr^{-1}$. The second highest range of frequencies was concentrated around 1020–1322 mm $yr^{-1}$, representing the majority of agricultural land. The consumptive water use of the different land cover types in study area indicated that irrigated cropland which occupied 14.6% of the study area had AET rates much higher than other land uses. Water bodies are the next highest, with forest and shrubland and sparse vegetation slightly lower, and very low AET rates from bare soil. Daily and seasonal water consumption of major cropping systems varied spatially depending on cropping practices and climatic conditions.



## 1. Introduction

The Kingdom of Saudi Arabia (KSA) has a modern agricultural sector with more than 1,348,696 (2013) hectares of irrigated land (Department of Statistics and Information, 2013). Almost all of the agricultural production areas are dependent on groundwater pumping for irrigation, which is challenging and costly (Mahmoud, 2014; Mahmoud et al., 2014). Agricultural water demand in KSA was about 83–90% of the total water demands of the country during 1990–2009 (Chowdhury and Al-Zahrani, 2015). For better assessment and management of irrigation water requirements, the estimation of consumptive use of water for agriculture is important as it is the main consumer of water in KSA. As large amount of irrigated water is lost through evapotranspiration (ET), therefore, accurate estimation is imperative for efficient management of irrigation water (Hafeez and Khan, 2005). Improved irrigation water management requires accurate scheduling of irrigation, which in turn requires an accurate calculation of daily ET (Bausch, 1995). Quantification of actual evapotranspiration from spectral satellite data requires determination of the Surface Energy Balance components with the support of field observations. Over the past decades, a large amount of research in hydrology has been directed to accurately estimate evapotranspiration rates at various spatial and temporal scales. One of the most important recent developments in the field of remote hydrological sensing is the determination of evapotranspiration (AET) rates from spectral satellite data based on an energy balance approach (Menenti, 1984; Parodi, 1993; Bastiaanssen, 1995; Bastiaanssen et al., 1998a).

* Corresponding author.
*E-mail addresses:* shmahmoud@ksu.edu.sa, eng.shereif1@hotmail.com (S.H. Mahmoud).

http://dx.doi.org/10.1016/j.jseaes.2016.05.012
1367-9120/

Surface Energy Balance Algorithm for Land Method (SEBAL) (Bastiaanssen, 1995) enables the calculation of actual and potential evapotranspiration during the day of the satellite recordings. The method involves complex procedures and determination of a number of variables from the different spectral bands of the satellite data, such as surface kinetic temperature, Normalized Difference Vegetation Index (NDVI), emissivity and albedo. Bastiaanssen (1995) described the method in detail. The widely adopted SEBAL model was mostly applied to agricultural areas (Bastiaanssen et al., 2005) where the flat landscape minimizes the spatial heterogeneities of the energy fluxes if compared to the effects of topography on meteorological variables. For these agricultural contexts, numerous applications can be found in the literature (Bastiaanssen, 2000; Choi et al., 2009; Minacapilli et al., 2009; Timmermans et al., 2007) mainly focusing on the validation of model outputs at a platform overpass time by means of simultaneous micro-meteorological measurements. Additionally, some applications are extended to regional (Sánchez et al., 2008) or basin (Teixeira et al., 2009) scales, by modifying the assessment of instantaneous fluxes to take into account the effects of complex topography.

Throughout the last decade, a growing number of satellite algorithms built on the Surface Energy Balance equation have been developed to estimate actual areal-averaged evapotranspiration by incorporating remotely sensed variables such as land surface temperature (LST), surface albedo, vegetation cover fraction, and land cover type in conjunction with field observations (Bastiaanssen, 2000; Morse et al., 2000; Boronina et al., 2005; Ahmad et al., 2005; Chemin and Honda, 2006; Senay et al., 2007; Wang et al., 2007; Singh et al., 2008; Elhaddad et al., 2010; Droogers et al., 2010; Liu et al., 2010; Li and Zhao, 2010; Santos et al., 2010; El Tahir et al., 2011; Sun et al., 2011; Mahmoud and Alazba, 2016). Wang et al. (2007) proposed a simple regression equation to estimate ET using surface net radiation, air, surface temperatures, vegetation indices, and ground-based measurements available at eight enhanced surface facility sites located throughout the southern Great Plains of the United States (U.S.A.). Their study concluded that AET can be reasonably predicted with a correlation coefficient that varied from 0.84 to 0.95 under a wide range of soil moisture conditions and land cover types. More recently, Singh et al. (2008) conducted a study to assess the operational characteristics and performance of the SEBAL model for estimating crop ET (ETc) and mapping spatial distribution and seasonal variation of ETc on a large scale in southcentral Nebraska, U.S.A. climatic conditions. The results of their study showed that the model was able to predict growing season cumulative daily maze (corn) ET reasonable well within 5% of the measured values. Additionally, they concluded that SEBAL can be a viable tool for generating ETc maps to assess and quantify the spatiotemporal distribution of ET on large scales as well as estimating surface energy fluxes. Elhaddad et al. (2010) used the energy balance-based model to estimate the spatial and temporal variability of AET in the Arkansas River Basin and South Platte River Basin, Colorado, U.S.A. and Palo Verde Irrigation District in California, U.S.A. along with a 1-day ET estimate for the Texas, U.S.A. Liu et al. (2010) estimated AET and determined the variation of varied land use types and land cover in urban settings. They implemented SEBAL model to estimate AET at a higher spatial resolution using Landsat 5 satellite images and field observations. Their results revealed that the lowest observed AET was for developed urban areas and the highest for open water bodies. The results of the above studies indicated that agricultural areas have higher AET values than urban for all land cover types except for open water bodies.

SEBAL has been tested under several irrigation schemes in Egypt, India, Sri Lanka, Pakistan, Afghanistan, Argentina, Turkey, Niger, China, Brazil, United States, Sudan, and Spain to diagnose the uniformity in crop consumptive use, crop water stress and irrigation performance (Bastiaanssen et al., 1998a,b; Wang et al., 1995; Bastiaanssen, 2000; Senay et al., 2007; Droogers et al., 2010; Li and Zhao, 2010; Santos et al., 2010; Bastiaanssen et al., 2012; Wu et al., 2015). The first attempt to assess actual irrigation applications based on remotely sensed evapotranspiration observations was by Ramos et al. (2006). These authors used the SEBAL model to assess the actual evapotranspiration and to compute net water volumes and net irrigation volumes by introducing a water application efficiency factor. They concluded that it is possible to assess actual irrigation applications based on actual evapotranspiration observations. A similar study conducted by Senay et al. (2007) using simplified Surface Energy Balance model to monitor and assess the performance of irrigated agriculture in Afghanistan using a combination of 1-km thermal data and 250 m Normalized Difference Vegetation Index (NDVI) data, both from the Moderate Resolution Imaging Spectroradiometer (MODIS) sensor. Seasonal AET over a period of six years for two major irrigated basins were computed by analyzing up to 19 cloud-free thermals and NDVI images from each year. Senay et al. (2007) reported that one of the major advantages of the energy-balance approach is that it can be used to quantify the spatial extent of irrigated fields and their water-use dynamics without reference to the source of water as opposed to a water balance model which requires knowledge of both the magnitude and temporal distribution of rainfall and irrigation rates applied to fields.

In the present study, spatial and temporal distribution of actual evapotranspiration over the western and southern regions of KSA during 1992–2014 are estimated using the Surface Energy Balance based algorithm with support of field observations in order to understand the distribution of AET over various land types. The zonal statistics for each kind of land-cover type was also carried out in order to understand water consumption of different land-cover types. Additionally, daily and seasonal water consumption for major crops (zucchini, wheat, tomatoes, sorghum vulgare, radish, pumpkin, potato, pomegranate, piper, peaches, date palm, millet, mango, lima bean, lettuce, grapefruit, grape, corn, carrots, barley, aubergine, apricot, apple, alfalfa, watermelon) were computed for western and southern regions of KSA.

## 2. Material and methods

### 2.1. Description of the study area

The present study was conducted in the southern and western regions of the KSA in five provinces (Fig. 1). The southern regions include, (1) Jazan Province, which is the smallest region of KSA. This province stretches 300 km along the southern Red Sea coast, north to Yemen. It covers an area of 12,435 km$^2$. Jazan Province also consists of over 100 islands in the Red Sea. Jazan Province has a hot desert climate with an average annual temperature of 30 °C. The weather varies from extremely hot during long summers to hot during short winters. Rainfall ranges between 70 and 270 mm yr$^{-1}$. (2) Al-Baha Province is situated in Hejaz Region of western KSA. It is the smallest of the KSA provinces covering 12,000 km$^2$. The climate of Al Baha Province is greatly influenced by its varying topography. Climate is generally moderate in summer and cold in winter with average temperatures ranging between 12 and 23 °C. The average rainfall throughout the entire province ranges 100–250 mm annually. (3) Asir Province is situated on a high plateau that receives more rainfall than the other areas of KSA and includes the country's highest peaks several rising to almost 3000 m at Jebel Sawdah near Abha. Asir Province occupies an area of 78,162 km$^2$. The dramatic increase in elevation of

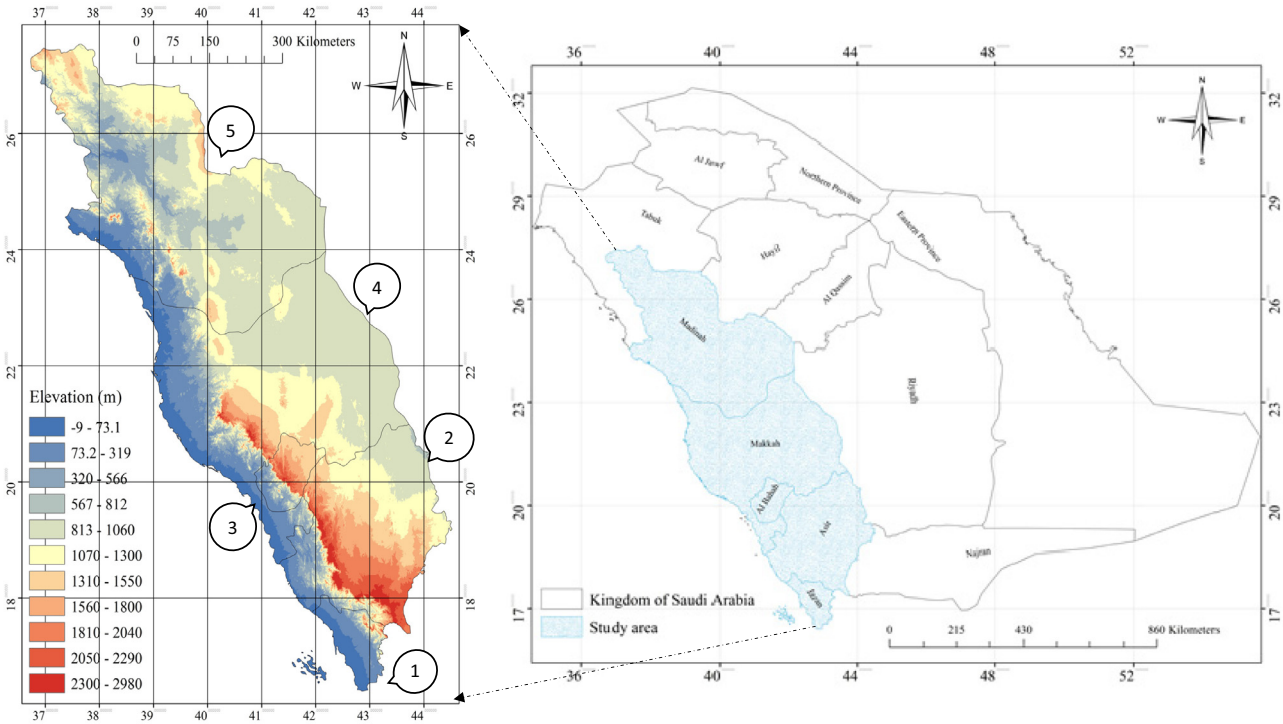


**Fig. 1.** Location map of the study area.

the Asir Mountains influences the amount and geographical distribution of rainfall in the region.

Western regions of KSA include the (4) Makkah Province and (5) Al-Madinah Province (Fig. 1). Makkah Province is located in western KSA and has an extended coastline. It has an area of 136,867 km$^2$ and a population of approximately 6,915,006. The geomorphology of the region has controlled the unique urban pattern of the Makkah metropolitan city. The sprawl of the city has followed a radial pattern on the limited surface areas of the complex alluvial channels separated by the steep mountain ranges. Occasional heavy storms cause severe flash flooding that can impact inhabited areas. The mean annual rainfall of Makkah Province ranges from 99 to 202 mm yr$^{-1}$. Al-Madinah Province has a coastal extent along the Red Sea of approximately 200 km on its western border. The entire region is covered with hills, hillocks, wadis, rock formations, and lava fields. The Province has an area of 146,669 km$^2$ and a population of 1,777,973.

Mean annual rainfall in the study area ranges from 36 to 332 mm yr$^{-1}$. The spatial distribution of mean annual rainfall in the entire study area indicated a large variation due to the considerable differences in topography and climate. The largest rainfall was observed in the mountainous area of Asir, Jazan, Al-Baha, and Makkah provinces (Fig. 2). Whereas the lowest mean annual rainfall of the study area was observed in Al-Madinah Province. Fig. 2 also shows the effect of topography on the mean annual rainfall. The profile indicates significant difference of the mean annual rainfall (36–332 mm yr$^{-1}$) between lowlands (mainly bare soil, urbanized areas) and highlands (which is mainly irrigated cropland and forest).

### 2.2. Reference evapotranspiration

Climatic data obtained from Meteorological Department, Ministry of Agriculture and Ministry of Water and Electricity. Reference evapotranspiration is the evapotranspiration from a hypothetical surface. In the case of the United Nations Food and Agriculture Organization (FAO) method (Monteith, 1965), this surface consists of reference crop with crop height of 0.12 m, which is actively growing and adequately watered. It has a surface roughness of 70 (s m$^{-1}$) and an albedo of 0.23. The latent heat flux of this reference surface is estimated according to the Penman– Monteith equation. In this study, 63 years of daily climate data (1992–2014) collected from weather stations located across the study area were used. Penman-Monteith method (Monteith, 1965) was used for estimating $ET_O$ on a grid-by-grid basis using Eq. (1).

$$\mathrm{ETo} = \frac{0.408\Delta(Rn - G) + \gamma\frac{900}{T+273}u_2(e_s - e_a)}{\Delta + \gamma(1 + 0.34u_2)} \quad (1)$$

where

ETo = reference evapotranspiration (mm/day),
Rn = net radiation at the crop surface (MJ/m$^2$/day),
G = soil heat flux density (MJ/m$^2$/day),
T = mean daily air temperature at 2 m height (°C),
$u_2$ = wind speed at 2 m height (m/s),
$e_s$ = saturation vapor pressure (kPa),
$e_a$ = actual vapor pressure (kPa),
$\Delta$ = slope vapor pressure curve (kPa/°C),
$\gamma$ = psychrometric constant (kPa/°C),
$e_s - e_a$ = saturation vapor pressure deficit (kPa).

The data include elevation, latitude and longitude of the station, total monthly rain, maximum and minimum air temperature, relative humidity, wind speed at 2 m height, and daily sunshine hours. Penman-Montieth calculations were implemented within the main program of GIS. Prior to calculating evapotranspiration, the Inverse Distance Weighted (IDW) interpolation function was utilized to interpolate the values of the input data for each Julian day throughout the year. Moreover, IDW interpolation function was utilized to interpolate each month, with the result being twelve separate maps of mean monthly ETo (mm/day).

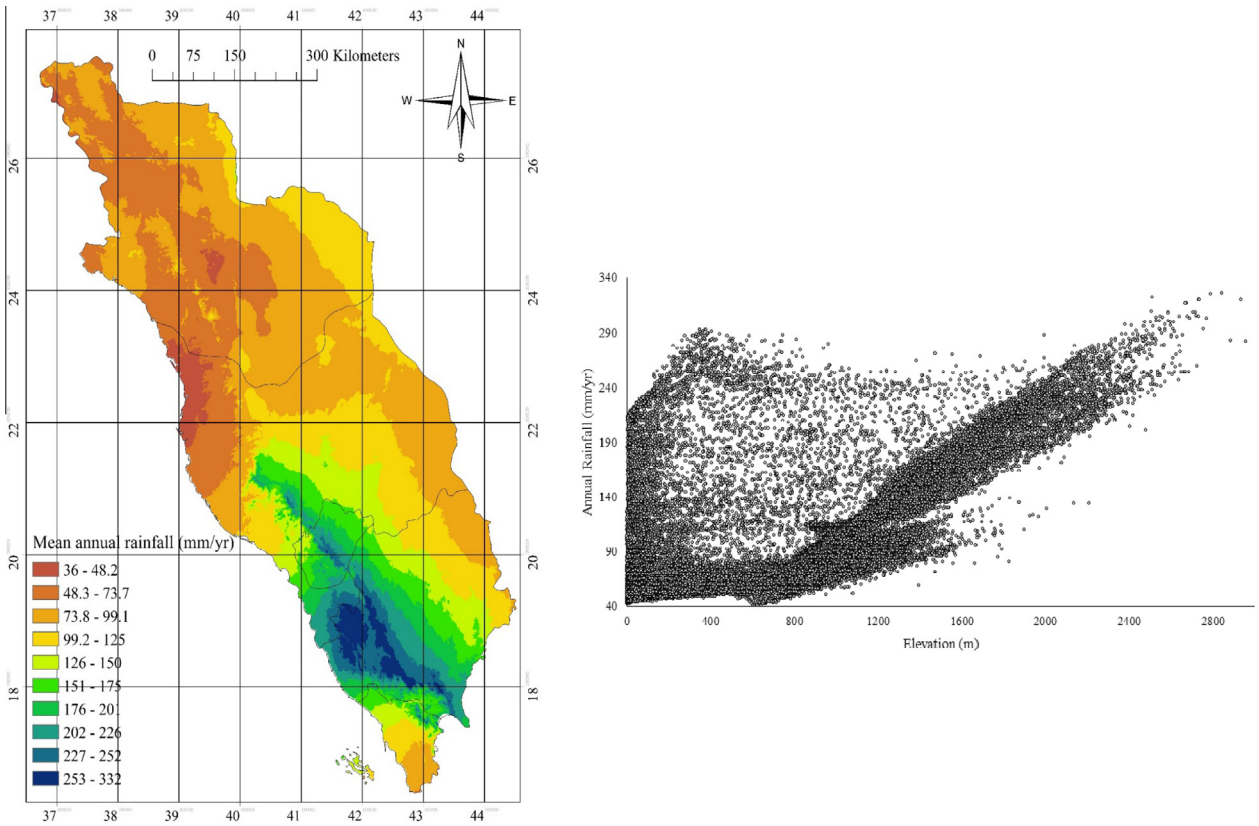


**Fig. 2.** Mean annual rainfall (1960–2014).

### 2.3. The SEBAL model

Actual evapotranspiration retrieval, either by means of remote sensing-based approaches or by micro-meteorological measurements, is based on the application of the Surface Energy Balance equation to the soil–plant–atmosphere system. SEBAL is one of the residual methods of energy budget, developed by Bastiaanssen et al. (1998a). It combines empirical and physical parameterization. This study was a multidisciplinary investigation involving a field survey and modeling. A variety of techniques such GIS, RS, and aerial image interpretation were used. The computational steps used to obtain AET are presented in Fig. 3. The remote sensing data used in this study includes MODIS atmospheric profile data (MOD07). Near surface temperature values are extracted at the pressure level closest to the ground-surface described by the region's digital elevation model (DEM), daily data were averaged to generate monthly averages. Data were further improved by relating MODIS-Ts to climate-station temperatures MODIS land surface temperature data (MOD11A2). Emissivity was derived by averaging MODIS-bands 31 and 32 emissivities, Normalized Difference Vegetation Index (NDVI) (MOD13Q1), MODIS products combined with BRDF-albedo products (MCD43B3). Shuttle Radar Topographic Mission DEM (gap-filled) obtained from the consortium of spatial data and information (Reuter et al., 2007). The inputs also include local weather data and satellite data. From the input data, the *Rn* (net solar radiation), NDVI, albedo, roughness length, and *G* (soil heat flux) are calculated. The Solar Analyst tool in ESRI's ArcGIS-environment was used to model solar radiation (Fu and Rich, 1999). The tool is capable of generating both point and area-integrated estimates of solar radiation for variable time intervals. This balance under the hypothesis that advection, energy required for photosynthesis and canopy and air storages are negligible, can be written as:

$$\lambda ET_{ins} = R_n - G - H \tag{2}$$

where $R_n$ (W m$^{-2}$) is the net radiation, G (W m$^{-2}$) is the soil heat flux at the surface, H (W m$^{-2}$) is the sensible heat flux and $\lambda ET_{ins}$ (W m$^{-2}$) is the latent heat flux, which represents the energy amount used for the surface evaporation and plant transpiration processes. The instantaneous Surface Energy Balance, Eq. (2), at satellite overpass time is solved for $\lambda ET_{ins}$ by applying a residual approach. In the framework of SEBAL modeling, the net radiation, Rn computed based on the balance between downwelling and upwelling shortwave and long-wave radiation: The equation to calculate the net radiation flux is given by

$$Rn = (1-\alpha)Rs_{\downarrow} - Rl_{\downarrow} - Rl_{\uparrow} - (1-\varepsilon_o)Rl_{\downarrow} \tag{3}$$

where Rn is the net radiation at the surface, $\alpha$ is the surface albedo, $Rs_{\downarrow}$ is the incoming short-radiation, $Rl_{\downarrow}$ is the incoming long-wave radiance, $Rl_{\uparrow}$ is the outgoing long-wave radiation, and $\varepsilon_o$ is the surface emissivity. Albedo is the ratio of reflected light to total incident sunlight for a given area of the land surface. It is a fundamental property controlling the energy flux at the surface of the Earth; it can provide information on the biophysical characteristics of the land surface including the structure of vegetation canopies, soil moisture, and urbanization. Broadband albedos are calculated using spectral-to-broadband conversion algorithms (Liang, 2000, 2003). The MODIS albedos represent the best quality data possible for each 16-day period (Zhou et al., 2003). Wanner et al. (1997) provide a detailed description of the MODIS albedo product, its creation, and validation. These products were developed based on atmospherically corrected, cloud-cleared reflectance observations from the MODIS sensors on NASA's Aqua and Terra satellites.

Digital elevation model (DEM) based methods to estimate net shortwave radiation prove sound for clear sky conditions (Ruiz-Arias et al., 2009). In this paper, we use the Solar Analyst tool in

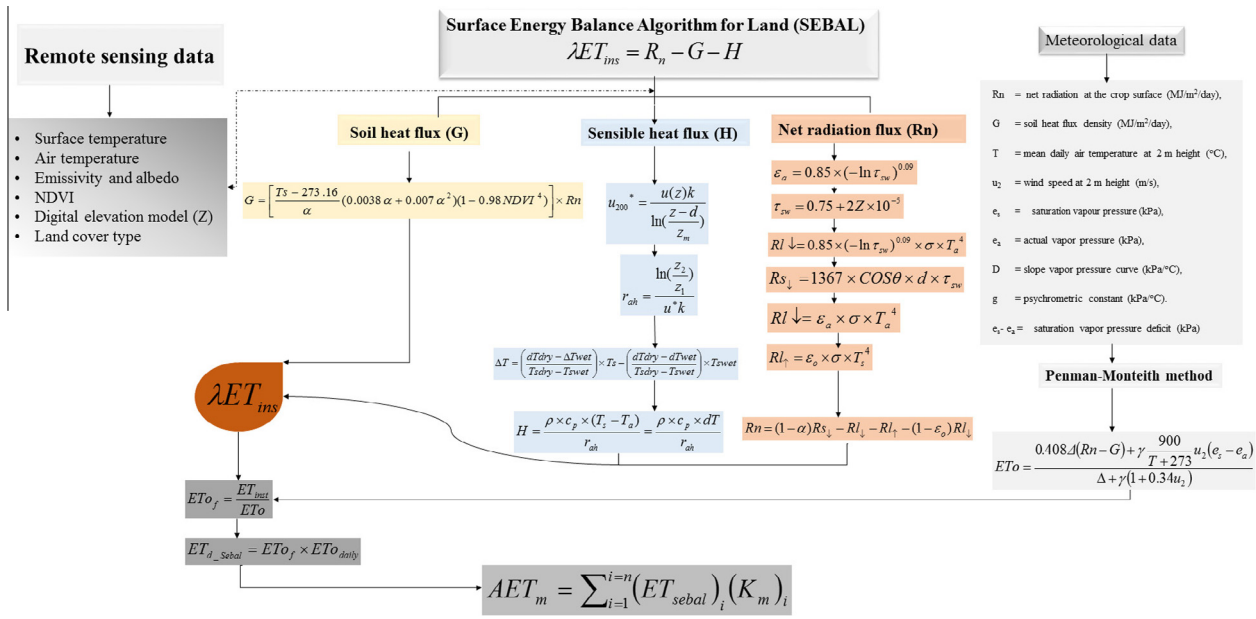


**Fig. 3.** Flowchart of computational steps used to obtain AET.

ESRI's ArcGIS-environment to model solar radiation. The tool is capable of generating both point and area-integrated estimates of solar radiation for variable time intervals.

$$Rs_{\downarrow} = 1367 \times \cos\theta \times d \times \tau_{sw} \tag{4}$$

where $\cos\theta$ is the cosine of the solar incidence angle, $d$ is the inverse squared relative earth-sun distance, and $\tau_{sw}$ is the atmospheric transmissivity. The atmospheric transmissivity values determined based on clear sky and relatively dry conditions obtained by using an elevation-based relationship $\tau_{sw} = 0.75 + 2Z \times 10^{-5}$ (Allen et al., 1998), where Z is the elevation of the weather station above sea level (m).

The incoming long-wave radiance $Rl_{\downarrow}$ and the outgoing long-wave radiation $Rl_{\uparrow}$ are derived from an application of the Stefan–Boltzmann equation and MODIS-based Ts and Ta as input, i.e.

$$Rl_{\uparrow} = \varepsilon_o \times \sigma \times T_s^4 \tag{5}$$

$$Rl\downarrow = \varepsilon_a \times \sigma \times T_a^4 \tag{6}$$

where $T_s$ is the mean surface temperature (K), which is obtained from the satellite data. Daily Ts data were averaged to generate monthly averages. Data were further improved by relating MODIS-Ts to climate-station temperatures.

$\sigma$ is the Stefan Boltzmann constant ($5.67 \times 10^{-8}$ W m$^{-2}$ K$^{-2}$), $\varepsilon_o$ is the broad-band surface emissivity, the surface emissivity was computed using an empirical equation where the NDVI > 0 by inputting the NDVI and the LAI as described in the SEBAL user manual, $\varepsilon_a$ is the emissivity of the atmosphere, emissivity of the atmosphere was calculated from Eq. (8).

$$\varepsilon_a = 0.85 \times (-\ln \tau_{sw})^{0.09} \tag{7}$$

Substituting (8) into (7) provides the following Eq. (8)

$$Rl\downarrow = 0.85 \times (-\ln \tau_{sw})^{0.09} \times \sigma \times T_a^4 \tag{8}$$

Soil heat flux cannot be directly determined from satellite sensors and requires empirical formulation. Remote sensing derivable parameters that influence soil heat flux are used; these include NDVI, surface temperature and albedo. The soil heat flux (G) has been estimated using the following relation developed by Bastiaanssen (1995):

$$G = \left[\frac{Ts - 273.16}{\alpha}(0.0038\alpha + 0.007\alpha^2)(1 - 0.98NDVI^4)\right] \times Rn \tag{9}$$

Sensible heat flux is the rate of heat loss to the air by convection and conduction, due to a temperature difference. It is computed using the following equation for heat transport:

$$H = \frac{\rho \times c_p \times (T_s - T_a)}{r_{ah}} = \frac{\rho \times c_p \times dT}{r_{ah}} \tag{10}$$

where $\rho$ is the air density (kg m$^{-3}$), $c_p$ is the specific heat of air (1004 J kg$^{-1}$ k$^{-1}$), $dT$ is the near surface temperature difference (K), $r_{ah}$ is the aerodynamic resistance to heat transport (s/m), where

$$\Delta T = \left(\frac{dTdry - \Delta Twet}{Tsdry - Tswet}\right) \times Ts - \left(\frac{dTdry - dTwet}{Tsdry - Tswet}\right) \times Tswet \tag{11}$$

The aerodynamic resistance to heat transport ($r_{ah}$) is computed for neutral stability as:

$$r_{ah} = \frac{\ln\left(\frac{z_2}{z_1}\right)}{u^* k} \tag{12}$$

$Z_1$ is a height just above the zero displacement distance height of plant canopy set to 0.1 m for each pixel, and $Z_2$ is the reference height just above the plant canopy set to 2 m for each pixel, u* is the friction velocity (m/s), and k is the von Karman constant (0.4).

$$u^* = \frac{u(z)k}{\ln\left(\frac{z-d}{z_m}\right)} \tag{13}$$

Surfaces of wind-velocity generated by interpolating climate-station recorded wind velocities. Inverse Distance Weighted (IDW) method was used to interpolate wind velocity at 2-m above the ground surface from climate-station recorded data. Elevation differences were used as weights in the interpolation of wind velocity. The initial value for friction velocity (u*) computed for neutral stability with data from the local meteorological station. The average height of vegetation (m) was surveyed in the site nearby the meteorological station and was used to calculate the land surface friction, Zm. Then, Zm for each pixel calculated by a regression equation according to the pixel NDVI value. The near-surface wind speed was converted to a value at the blending height (200 m) where the effects from the land surface roughness could

**Table 1**
Areal distribution of different land cover classes.

| Land cover class | Area (%) | Area ($km^2$) |
|---|---|---|
| Irrigated cropland | 14.62 | 23580.2 |
| Forest and shrubland | 0.56 | 904.3 |
| Sparse vegetation | 4.73 | 7622.4 |
| Bare areas | 80.03 | 129092.14 |
| Water bodies | 0.06 | 93.3 |

be eliminated. The initial estimated values of $u^*$ were used to infer the first values of aerodynamic resistance ($r_{ah}$). Corrections for atmosphere stability were obtained iteratively for each pixel. It required a series of iterations to determine new values of the corrected friction velocity and the corrected aerodynamic resistance before obtaining numerical stability based on the criterion of Monin–Obukhov length (Monin and Obukhov, 1954).

Once Sensible heat flux and the available energy (Rn-G) are determined, estimation of instantaneous $ET_{ins}$ was computed pixel by pixel using Eq. (2). The evaporative fraction (EF) describes the partitioning of the Surface Energy Balance as the latent heat flux/net available energy, with the net available energy being defined as the difference in net radiation and soil heat flux. In this study, we used the concept "ETo fraction" (EToF), which represents the ratio of ET of each pixel to the reference ET as computed by Penman-Monteith method. EToF is the same as the crop coefficient, Kc; and is calculated by applied using Eq. (14). Then, daily values of ET were computed using (15)

$$ETo_f = \frac{ET_{inst}}{ETo} \tag{14}$$

$$ET_{d\_Sebal} = ETo_f \times ETo_{daily} \tag{15}$$

The computation of the monthly AET involved extrapolating the SEBAL daily AET, within each month, proportionally to the reference evapotranspiration where the latter is derived from standard meteorological measurements. The procedure involves determining the cumulative reference evapotranspiration between successive satellite images before computing the ratio, (km) of the cumulative reference evapotranspiration ET to the average potential ET over the period. The monthly ET, ($AET_m$), was then computed as follows:

$$AET_m = \sum_{i=1}^{i=n} (ET_{sebal})_i (K_m)_i \tag{16}$$

## 3. Results and discussion

### 3.1. Developing land cover and reference evapotranspiration

A Landsat 5/7 TM/ETM images were obtained in 2014 from King Abdul-Aziz City for Science and Technology, KSA. This image incorporated with collected data from the specified region and ultimately utilized in categorizing land cover (LC). The extent of the

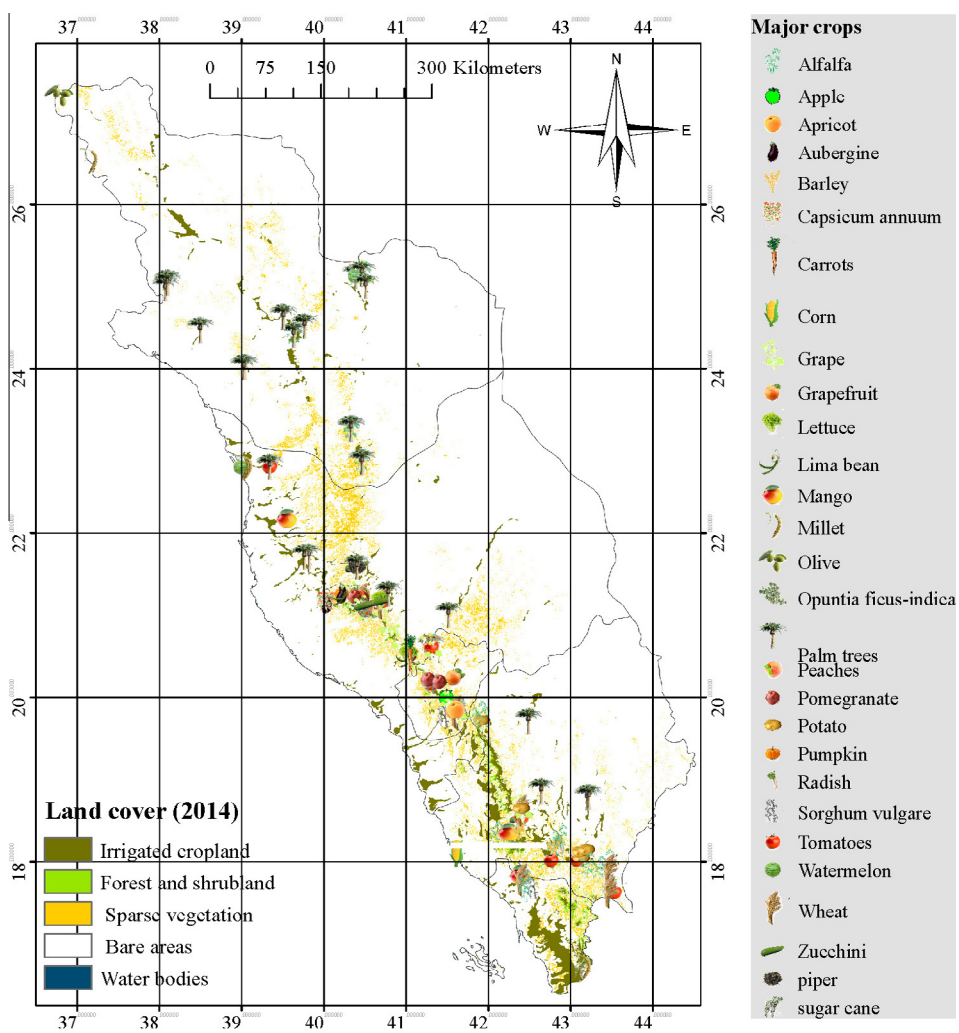


**Fig. 4.** Land cover map of the study area.

land cover distribution in 2014 is presented in Fig. 3. Fig. 3 also presents a database of 29 actual crop distributions over 754 sampling sites developed in ArcGIS 10.1 based on collected data. The database contains both actual crops (zucchini, wheat, tomatoes, sorghum vulgare, radish, pumpkin, potato, pomegranate, piper, peaches, date palm, millet, mango, lima bean, lettuce, grapefruit, grape, corn, carrots, barley, aubergine, apricot, apple, alfalfa, watermelon). This database also contains growing season dates. The areal extent of each class and its land cover are presented in Table 1. The western and southern regions occupy about 7.5% of the total area of KSA. These regions were selected for this study because of their total area of irrigated cropland, combining for almost 22% of the total area of irrigated cropland in KSA with an area of 23,580.2 $km^2$ (see Table 1) (see Fig. 4).

The spatial distributions of annual ETo are shown in Fig. 5, which reflects a combined effect of all climatological factors. There was large variation in ETo values due to the variation in meteorological variables from the different provinces caused the differences in seasonal variations of ETo. The lowest annual ETo values were from the mountainous areas of Asir, Jazan, Al-Baha, and Makkah provinces (1710–2058 mm $yr^{-1}$). The maximum values of ETo rates were from Al-Madinah Province (2059–2405 mm $yr^{-1}$), Makkah Province-except from mountains area (2059–2336 mm $yr^{-1}$), southwestern areas of Al-Baha Province (2128–2197 mm $yr^{-1}$) and northwestern areas of Asir Province (2127–2266 mm $yr^{-1}$). The results are promising and appear to provide comparable or be better estimates of ETo than currently available from PET methodologies that use ground based observations. Finally, the annual ETo indicates a high value from the entire study area, ranging from 1710 to 2405 mm $yr^{-1}$. Topography and climatic effects described the variation in annual ETo values. However, the differences in latitude seem to be more significant (73–2980 m) for the fluctuation of evapotranspiration in addition to the degree of aridity. Our results and mapping of ETo could be used for agro-climatic purposes and design.

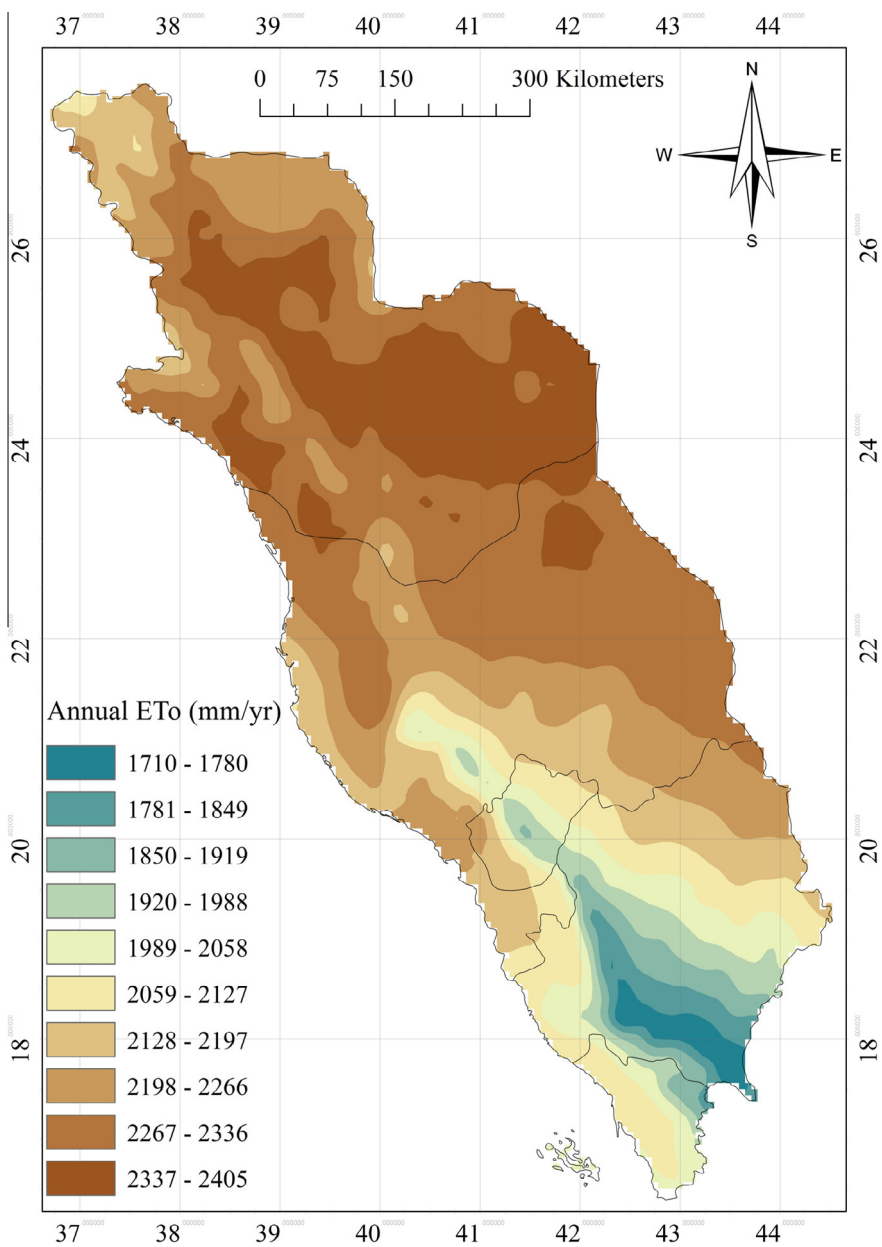


**Fig. 5.** Mean annual reference evapotranspiration (1992–2014).

### 3.2. Spatial–temporal distribution of monthly and annual AET

The AET layers defined the average (1992–2014) actual evapotranspiration (mm) of the different land uses on a monthly and annual basis. The highest monthly values (Fig. 6) were in April (4.97–49 mm/day), May (3.43–48.9 mm/day), and June (1.2–41 mm/day). The monthly distribution of AET showed a gradual increase from January to April. In January, daily AET ranged from 1 to 18.3 mm/day, with a mean of 6.16 mm/day and stander deviation (std) of 3.07 mm day$^{-1}$. In February, AET ranged from 2

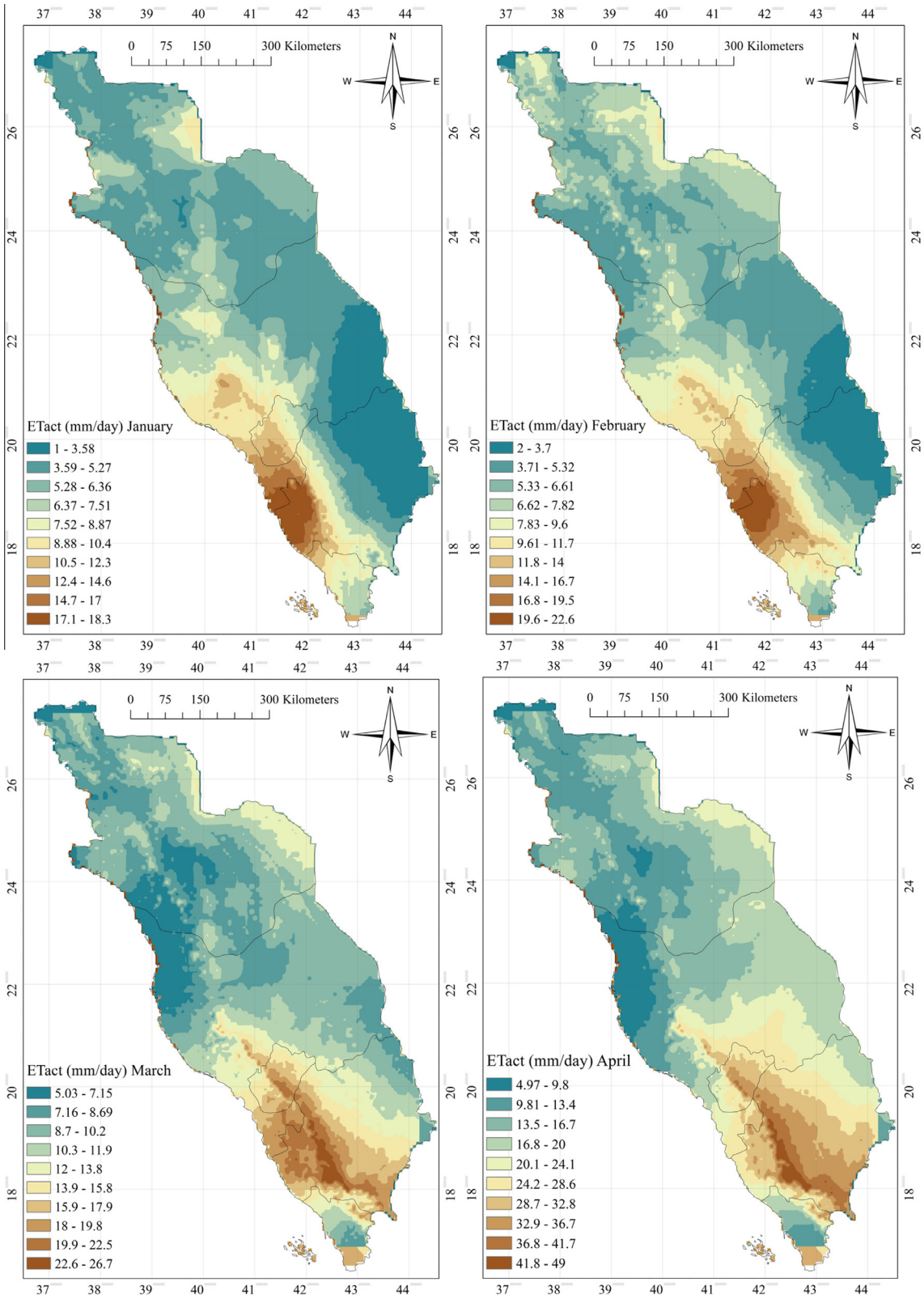


**Fig. 6.** Spatial distribution of average monthly actual evapotranspiration.

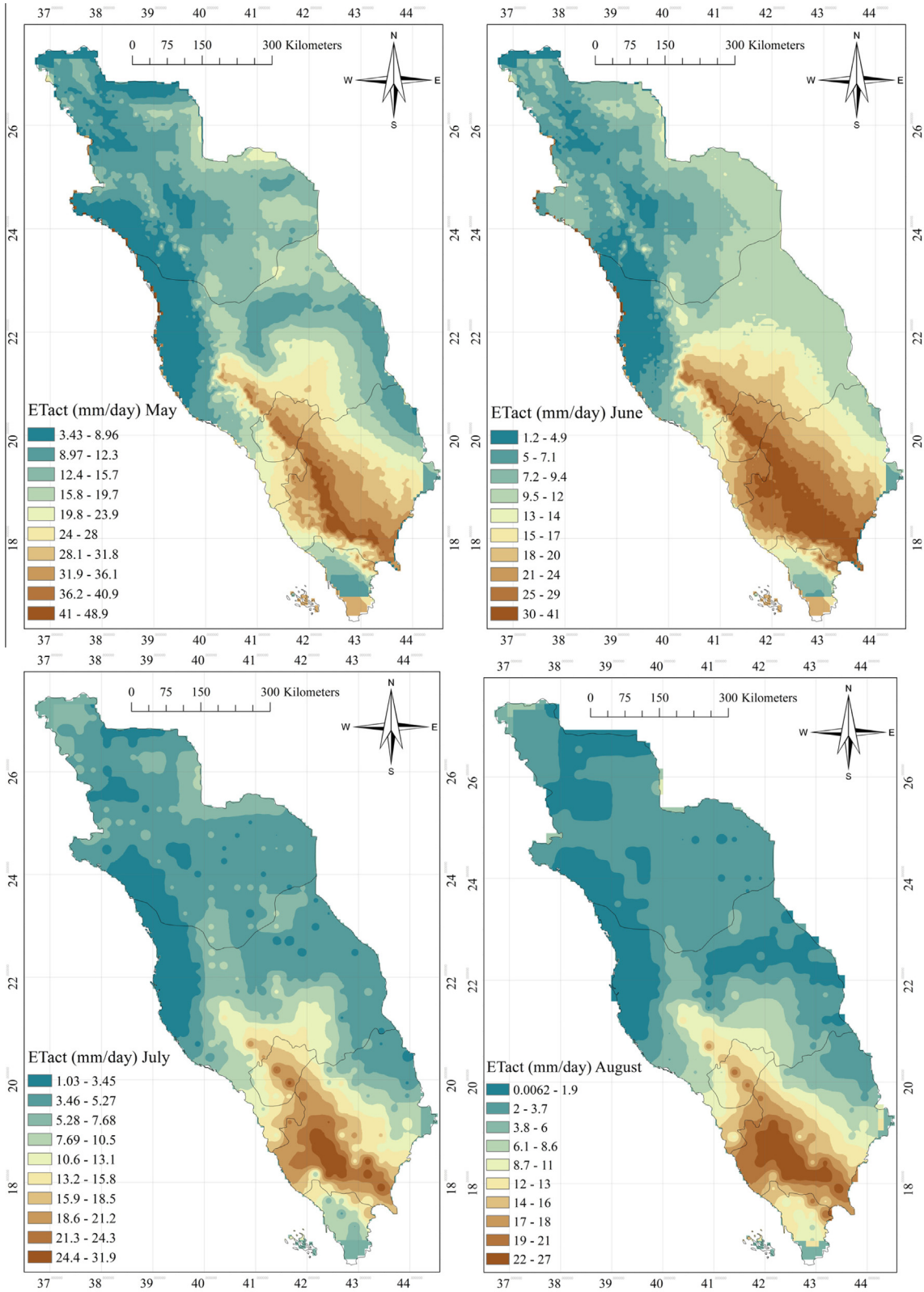


**Fig. 6** (*continued*)

to 22.6 mm/day with a mean of 7.01 mm/day and std equal 3.39 mm day$^{-1}$, in March, daily AET ranged from 0 to 26.73 mm/day, with a mean equal 10.89 mm/day and std = 3.88 mm day$^{-1}$, while the highest observed value in April ranged from 0 to 49 mm/day, and the mean daily AET is 19.09 mm/day with a std equal 7.85 mm day$^{-1}$. In contrast, there was a subsequent decline in daily AET values from May to December. In May daily AET ranged from 0 to 48.9 mm/day, and the mean daily value dropped to

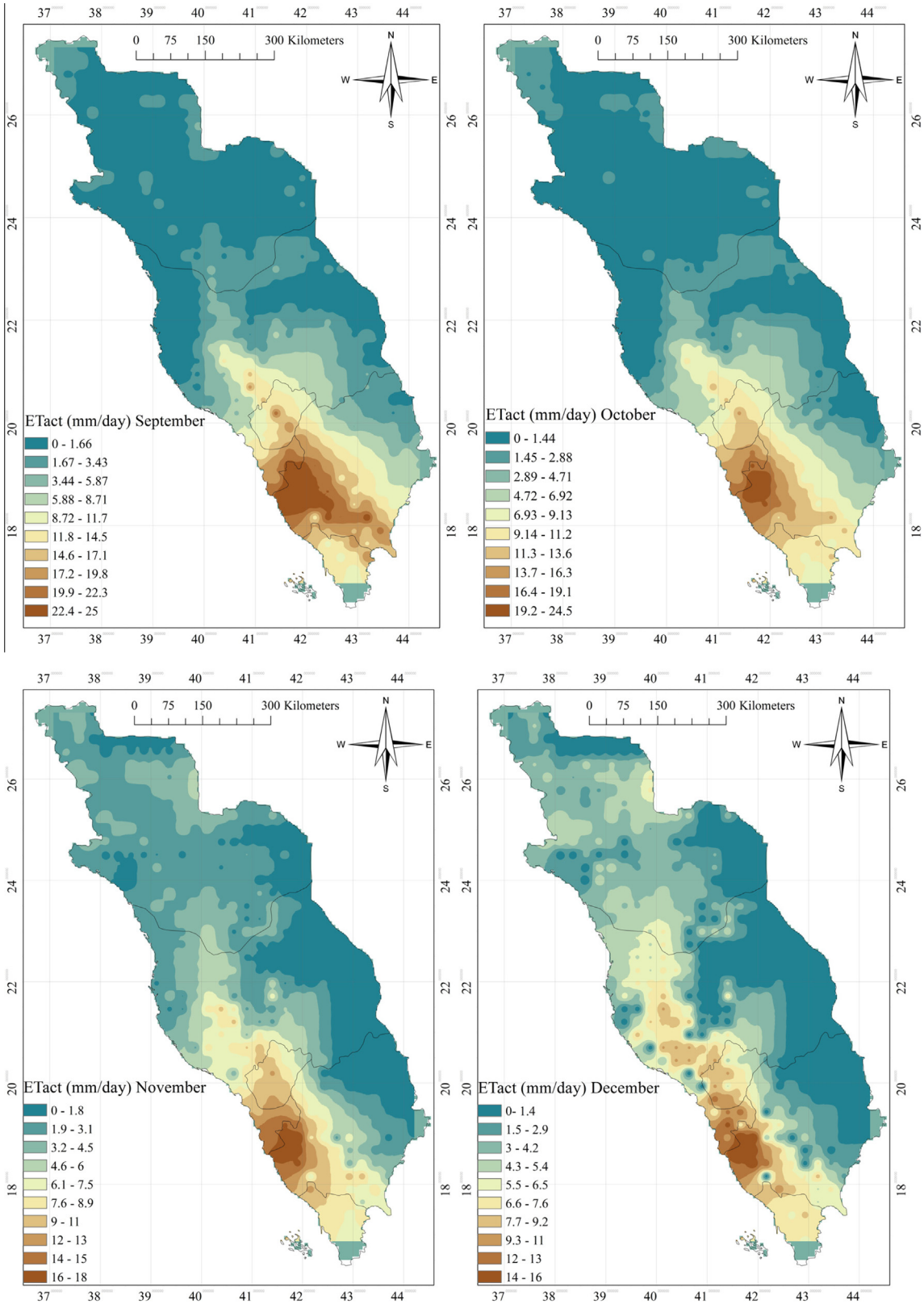


**Fig. 6** (*continued*)

17.16 mm/day with std equalling 8.8 mm day$^{-1}$. June daily values varied from 0 to 41.2 mm/day (mean = 12.6 mm/day and std = 7.5 mm day$^{-1}$). In July, daily AET ranged from 1.03 to 31.9 mm/day (mean = 7.7 mm/day and std = 5.6 mm day$^{-1}$), in August daily values varied from 0 to 27 mm/day (mean = 5.6 mm/day and std = 5.6 mm day$^{-1}$), in September daily AET ranged from 0 to 25 mm/day (mean = 5.1 mm/day and std = 6.17 mm day$^{-1}$), in October daily values ranged from 0 to 24.5 mm/day

(mean = 3.78 mm/day and std = 4.3 mm day$^{-1}$). The decline in daily AET values was clearly seen in November where the daily values ranged from 0 to 18 mm/day (mean = 3.9 mm/day, std = 3.03 mm day$^{-1}$) in addition the lowest observed daily AET was observed in December, ranging from 0 to 16 mm/day and the mean daily AET in this month was 3.6 mm/day. The lowest stand error deviation of daily AET values were in December, equalling 2.8 mm day$^{-1}$. The distribution and frequency of the estimated AET are given in Fig. 7. The normal distribution of the daily AET values is shown in Fig. 7. In January and February, values ranged from 4 to 6 mm/day fall within a large range of frequencies. Whereas in March, the highest range of frequencies for daily AET values were concentrated around 8–11 mm/day, representing the majority of the agricultural land in the study area. In April, the highest range of frequencies for daily AET were for values that ranged from 15 to 20 mm/day. In May, values ranged from 10 to 15 mm/day included the highest range of frequencies. The highest range of frequencies for daily AET in June-December were for values that ranged from 8–12 mm/day, 3–6 mm/day, 0–3 mm/day, 0–2 mm/day, 0–2 mm/day, 2–4 mm/day, and 0–2 mm/day, respectively.

The spatial variation of monthly AET over the entire study area is shown in Fig. 6. In general, all types of LC show similar seasonal dynamic trends for AET throughout the years. The value of AET began to rise rapidly in February, reached peak values in April, and then declined to the lowest levels in December. The maximum monthly AET values in the study area were observed for irrigated cropland and the mountains areas in the southwestern, central and southeastern areas of Asir Province, central and southwestern areas of Al-Baha Province, the irrigated areas in central and the plains area of Jazan Province, the southern portion of Makkah Province, and limited areas in the northern areas of Al-Madinah Province. Asir Province, which had the highest AET values during the year, is also one of the largest agricultural areas of southwestern KSA. Much of this arable and fertile land of this area is planted in date palm and under vegetables production. Irrigated cropland in the plains of Jazan and Al-Baha provinces, which included production of cereal grains (barley, millet and wheat) and fruit (apples, bananas, grapes, mangoes, papayas, plums and citrus) had a high AET value during the study period. The amount of monthly AET in these areas is of great concern as much water is

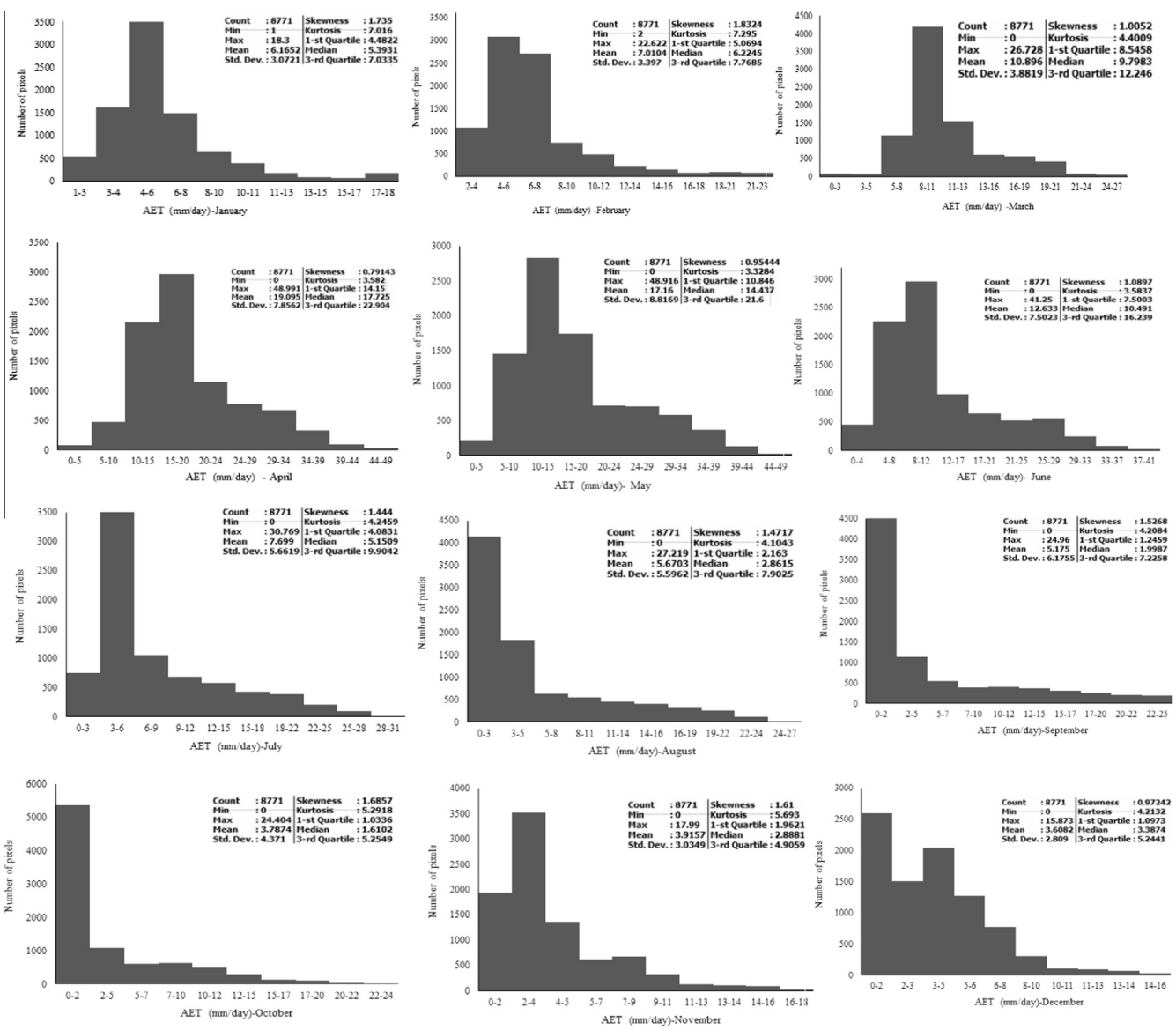


**Fig. 7.** Frequency distribution of average daily AET in the study area.

extracted from groundwater aquifers. Monthly AET of irrigated cropland depends on water availability and atmospheric water demand.

The annual AET ranged from 418.8 to 3442.3 mm $yr^{-1}$ with a mean annual value of 1256.4 mm $yr^{-1}$ and standard deviation equal 671.6 mm $yr^{-1}$. The modeled average annual AET by SEBAL model is presented in Fig. 8. The spatial distribution of annual AET shows moderate values in non-irrigated areas (414–948 mm $yr^{-1}$). Whereas it shows very high AET values in irrigated cropland and the mountain areas of the southwestern, central and southeastern areas of Asir Province, central and southwestern areas of Al-Baha Province, irrigated areas in central and the plains areas of Jazan Province, southern portion of Al-Makkah Province, and limited areas in the northern regions of Al-Madinah Province, where annual AET ranged from 1510 to 3430 mm $yr^{-1}$. Overall, the relatively large actual ET estimates due to several factors, which, included climate conditions, irrigation from groundwater wells, and the cropping pattern of these areas. The normal distribution of mean annual AET values is shown in Fig. 9. Values ranged from 717 to 1020 mm $yr^{-1}$ fall within a very large range of frequencies. Where 42% of the entire study area has an annual AET ranged from 717 to 1020 mm $yr^{-1}$ (see Fig. 10). The second highest range of frequencies for mean annual AET values is concentrated around 1020–1322 mm $yr^{-1}$, representing the majority of the study area agricultural land.

### 3.3. Daily and seasonal water consumption for major crops and land cover types

Fig. 11 indicates the average daily AET for different land uses in the study area. All types of LC showed similar monthly dynamic trends for AET throughout the years. The value of AET began to rise

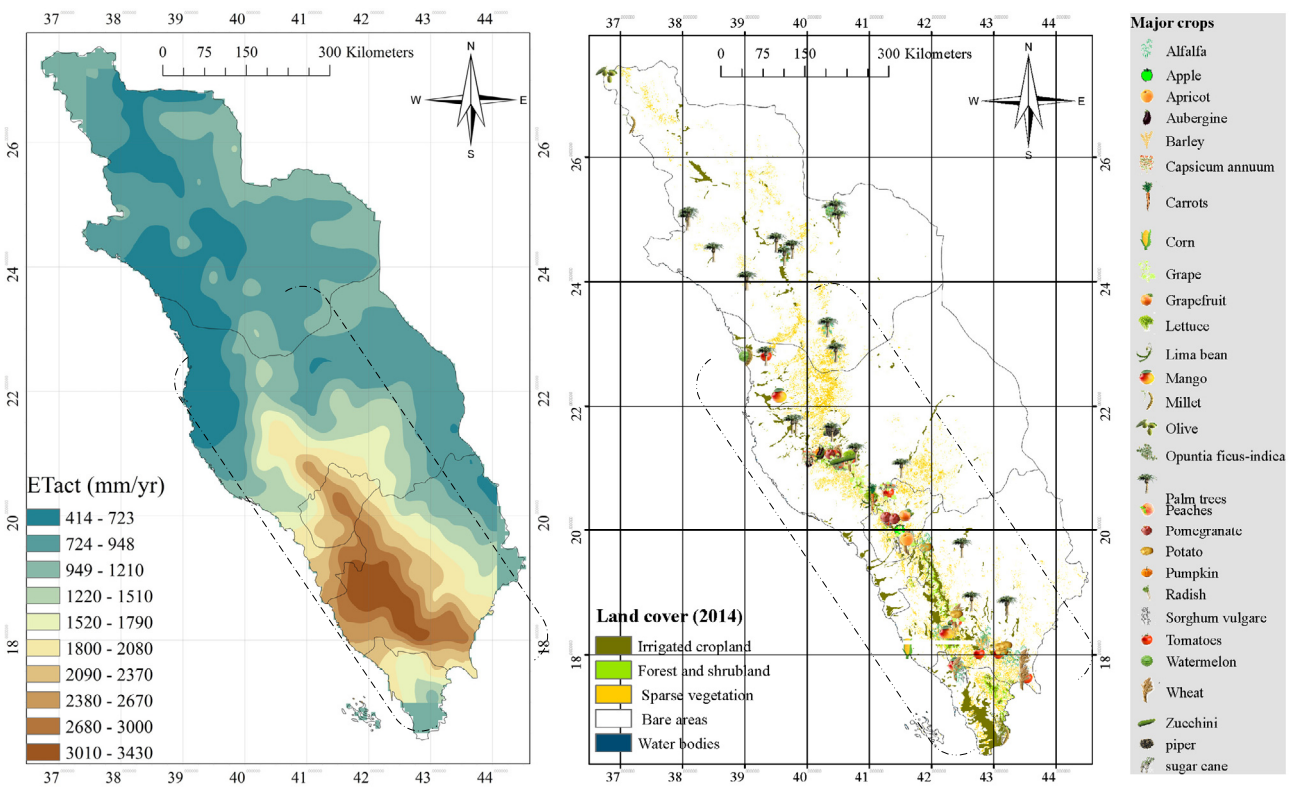


**Fig. 8.** Estimated mean annual actual evapotranspiration for the entire study area.

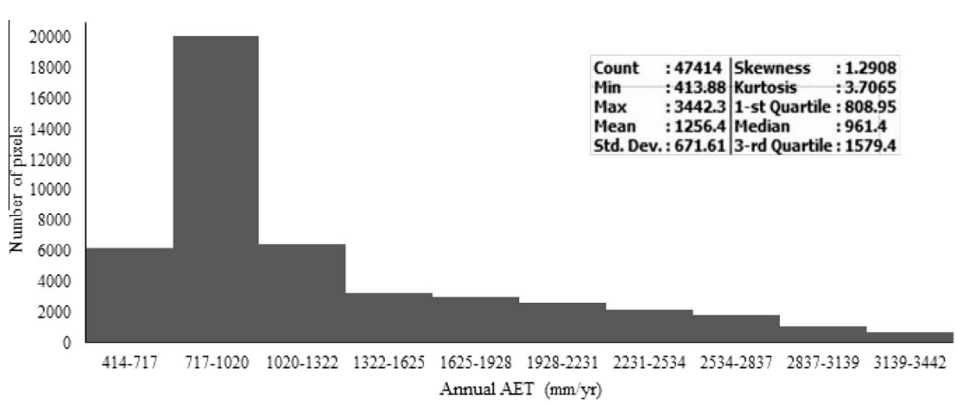


**Fig. 9.** Frequency distribution of mean annual AET in the study area.

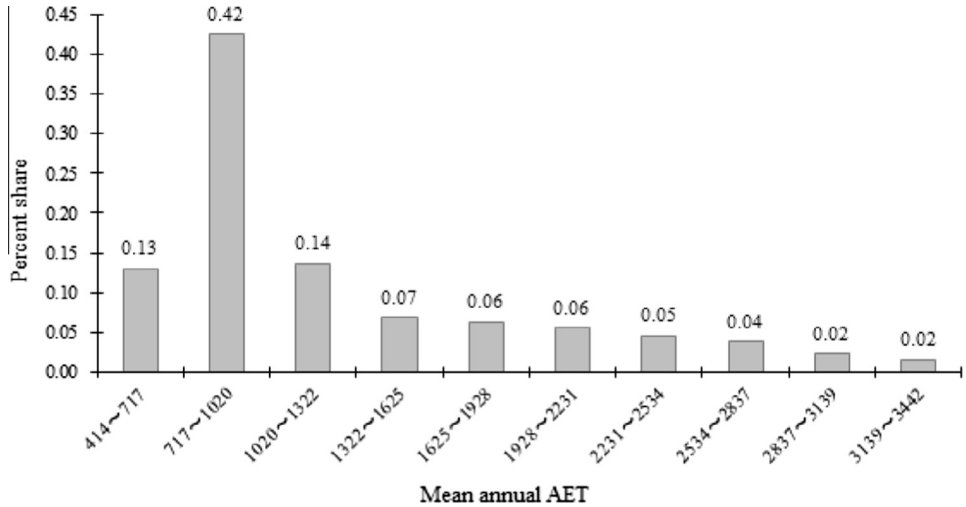


**Fig. 10.** Percent share of estimated mean annual actual evapotranspiration.

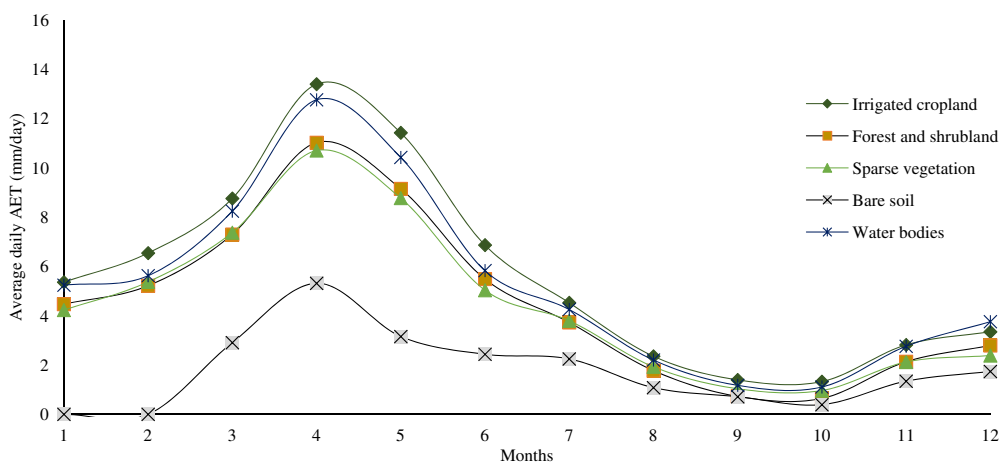


**Fig. 11.** Estimated average daily AET rates of different land uses including water bodies.

**Table 2**
Monthly and seasonal actual evapotranspiration of major crops in the study area.

| Crop | Jan. | Feb. | Mar. | Apr. | May | June | July | Aug. | Sept. | Oct. | Nov. | Dec. | Mean annual AET |
|---|---|---|---|---|---|---|---|---|---|---|---|---|---|
| | AET (mm/day) | | | | | | | | | | | | AET (mm/season) |
| Zucchini | – | – | – | – | – | – | – | – | 11.7 | 8.7 | 7.9 | 6.7 | 552.1 |
| Wheat | 9.6 | 11.2 | 18.2 | 32.7 | – | – | – | – | – | – | 8.7 | 7.3 | 744.7 |
| Tomatoes | 9.4 | 10.7 | 15.8 | – | – | – | – | – | – | – | 8.0 | 7.0 | 751.3 |
| Sorghum vulgare | – | 11.3 | 17.2 | 30.6 | 31.5 | 25.1 | 17.9 | 15.8 | 16.1 | 11.1 | 8.9 | 7.4 | 552.3 |
| Radish | – | – | – | – | – | – | – | – | 16.6 | 11.2 | 8.4 | 7.3 | 399.2 |
| Pumpkin | – | – | – | – | – | 17.2 | 8.7 | 6.6 | 6.2 | 5.5 | – | – | 474.7 |
| Potato | 8.6 | – | – | – | – | 34.8 | 26.3 | 23.2 | 21.7 | 12.7 | 9.1 | 7.3 | 863 |
| Pomegranate | 11.0 | 12.2 | 16.6 | 30.1 | 33.4 | 26.7 | 17.4 | 14.5 | 14.8 | 11.0 | 9.3 | 8.4 | 2197.2 |
| piper | – | – | – | – | – | – | – | – | 6.9 | 5.9 | 7.0 | 6.2 | 414.9 |
| Peaches | 11.8 | 12.7 | 14.2 | 25.8 | 30.0 | 23.8 | 11.4 | 9.4 | 9.3 | 8.1 | 7.5 | 6.5 | 1932.1 |
| Palm trees | 6.2 | 6.4 | 10.1 | 17.8 | 16.7 | 12.0 | 7.7 | 5.4 | 4.8 | 3.4 | 4.2 | 4.5 | 2976 |
| Millet | 7.4 | – | – | – | – | 8.7 | 5.4 | 4.3 | – | 3.0 | 4.5 | 5.8 | 597.9 |
| Mango | 9.3 | 9.4 | 12.0 | 18.2 | 16.5 | 12.1 | 10.6 | 9.4 | 9.9 | 7.2 | 7.2 | 8.0 | 1429.5 |
| Lima bean | – | – | 14.8 | 25.3 | 28.2 | 23.0 | 12.0 | 9.4 | 9.2 | – | – | – | 437.4 |
| Lettuce | – | 11.5 | 15.1 | 26.7 | – | – | 13.6 | 11.3 | 11.4 | 9.1 | 8.4 | 7.3 | 422.8 |
| Grapefruit | 10.5 | 11.7 | 18.3 | 32.5 | 34.8 | 27.9 | 19.5 | 15.6 | 16.1 | 11.7 | 9.5 | 7.8 | 2460.3 |
| Grape | 10.2 | 12.0 | 18.2 | 32.6 | 35.7 | 28.8 | 18.9 | 15.4 | 15.2 | 10.9 | 8.7 | 7.2 | 2417.6 |
| Corn | 18.3 | – | – | – | – | 17.5 | 19.5 | 18.8 | 21.5 | 16.8 | 12.9 | 11.2 | 652.1 |
| Carrots | – | 12.9 | 18.1 | 31.2 | – | – | – | – | – | – | – | – | 438.1 |
| Barley | 9.6 | 13.8 | 23.5 | – | – | – | – | – | – | – | 9.2 | 7.4 | 666.7 |
| Aubergine | – | – | – | – | – | – | – | – | 5.1 | 4.6 | 5.9 | 7.5 | 396.7 |
| Apricot | 10.4 | 12.5 | 20.7 | 36.4 | 38.4 | 31.3 | 20.3 | 16.3 | 17.3 | 12.3 | 9.7 | 7.7 | 2411.7 |
| Apple | 11.7 | 12.4 | 17.1 | 31.1 | 34.8 | 27.5 | 15.0 | 12.2 | 12.4 | 9.9 | 8.5 | 6.8 | 2247.8 |
| Alfalfa | 8.2 | 10.0 | 16.0 | 28.8 | 29.3 | 23.0 | 16.1 | 13.5 | 13.2 | 8.6 | 7.2 | 6.3 | 2127.0 |
| Watermelon | 5.0 | 6.2 | 10.8 | 16.7 | – | – | – | – | – | – | – | 3.8 | 487.5 |

(–) out of the growing seasons for these specific crops.

rapidly in February, reached peak values in April, and then declined to the lowest levels in December. These results indicated that bare soil has low values of AET, whereas irrigated cropland showed the highest values. In general, AET rates for irrigated cropland were much higher than for other land uses. Water bodies were the next highest, with forest and shrubland and sparse vegetation slightly lower, and very low AET rates from bare soil. There is little AET from the urban cover as the area is primarily non-vegetated. Irrigated cropland transpires at a slightly higher level than other vegetation, as they maintain a canopy cover throughout the year (Baron et al., 1998). The evaporative behavior or consumptive water use of the different land cover types in the study area as inferred by SEBAL model indicated that irrigated cropland which occupied 14.6% of the study area had an average daily AET that ranged from 6 mm/day in January, peaking in April (14 mm/day) and declined to 3 mm/day in December. Whereas water bodies, which covered 0.06% (93.3 $km^2$) of the study area, had also relatively high mean actual evapotranspiration. However, it covered only a limited area. In contrast, AET rates from water bodies were an indication of very high evaporative water from rainwater storage structures.

Estimating consumptive water use for agriculture in KSA has always been a challenge for agricultural producers, water managers, and government agencies. Quantification of consumptive use allows for more informed water use practices, consistent measures of the allocation among stakeholders, and improved planning. Herein, a database of 29 actual crop distributed over 754 sampling sites was developed in ArcGIS 10.1 based on collected data. The database contains both actual crops (zucchini, wheat, tomatoes, sorghum vulgare, radish, pumpkin, potato, pomegranate, piper, peaches, date palm, millet, mango, lima bean, lettuce, grapefruit, grape, corn, carrots, barley, aubergine, apricot, apple, alfalfa, watermelon). This database also contains growing season dates. Daily and seasonal water consumption for these crops were computed based on the developed AET layers and growing season dates. A summary of the values obtained for each crop is given in Table 2.

## 4. Conclusion

In the present study, spatial and temporal distribution of actual evapotranspiration over the western and southern regions of KSA during 1992–2014 were estimated using the Surface Energy Balance based algorithm with support of field observations, in order to understand the distribution of AET over various land types. The western and southern regions of KSA were selected in this study due to their total area of irrigated cropland as they share almost 22% of the total area of irrigated cropland in KSA with an area of 23,580.2 $km^2$. The developed AET layers defined the average actual evapotranspiration (mm) (1992–2014) of different land uses on monthly and annual basis. The highest monthly values were in April (4.97–49 mm/day), May (3.43–48.9 mm/day), and June (1.2–41 mm/day). The monthly distribution of AET showed a gradual increase from January to April. Otherwise, there was a subsequent decline in daily AET values from May to December.

The spatial variation of monthly AET over the entire study area indicates that all types of LC show similar seasonal dynamic trends for AET throughout the years. The value of AET started to rise rapidly in February, reached peak values in April, and then declined to the lowest levels in December. The maximum monthly AET values in the entire study area were observed in irrigated cropland and the mountain areas in the southwestern, central and southeastern regions of Asir Province, central and southwestern regions of Al-Baha province, central and the plains region of Jazan Province, southern portion of Al-Makkah Province, and limited areas in the northern regions of Madinah Province. The annual AET ranged from 418.8 to 3442.3 mm $yr^{-1}$ with a mean annual value of 1256.4 mm $yr^{-1}$ and stander deviation equal 671.6 mm $yr^{-1}$. Overall, the relatively large actual ET estimates, due to several factors, which, include climate conditions and irrigation from groundwater well, and cropping pattern in these areas. The normal distribution of mean annual AET values revealed that values ranged from 717 to 1020 mm $yr^{-1}$ fall within a very large range of frequencies. Forty-two percent of the entire study area had an annual AET that ranged from 717 to 1020 mm $yr^{-1}$. The second highest range of frequencies for mean annual AET values was concentrated around 1020–1322 mm $yr^{-1}$, representing the majority of the study area agricultural land. The consumptive water use of the different land cover types in the study area as inferred by SEBAL model indicated that irrigated cropland, occupying 14.6% of the study area, had an average daily AET that ranged from 6 mm/day in January to a peak in April (14 mm/day) and decreased to 3 mm/day in December. Whereas water bodies, which covered 0.06% (93.3 $km^2$) of the study area, had also relatively high mean actual evapotranspiration. AET rates from water bodies were an indication of very high evaporative water from rainwater storage structures and limited surface bonds. Estimating consumptive water use for agriculture in KSA has always been a challenge for agricultural producers, water managers, and government agencies.

## Acknowledgment

The authors would like to thank Professor Boris Kondratieff, Colorado State University, Fort Collins, CO, USA, for his suggestions and linguistic assistance. We are grateful to Prof. Dapeng Zhao, Associate Editor and the anonymous reviewers for their constructive feedback and thoughtful comments that improved the manuscript.

## References

Ahmad, M.U.D., Magagula, T.F., Love, D., Kongo, V., Mul, M.L., Kinoti, J., 2005. Estimating actual evapotranspiration through remote sensing techniques to improve agricultural water management: a case study in the transboundary Olifants catchment in the Limpopo Basin, South Africa.

Allen, R.G., Pereira, L.S., Raes, D., Smith, M., 1998. Crop evapotranspiration-guidelines for computing crop water requirements-FAO irrigation and drainage paper 56. FAO, Rome 300 (9), D05109.

Baron, J.S., Hartman, M.D., Kittel, T.G.F., Band, L.E., Ojima, D.S., Lammers, R.B., 1998. Effects of land cover, water redistribution, and temperature on ecosystem processes in the South Platte Basin. Ecol. Appl. 8 (4), 1037–1051.

Bastiaanssen, W.G.M., 1995. In: Regionalization of Surface Flux Densities and Moisture Indicators in Composite Terrain: A Remote Sensing Approach Under Clear Skies in Mediterranean Climates. Landbouwuniversiteit te Wageningen, p. 273.

Bastiaanssen, W.G.M., 2000. SEBAL-based sensible and latent heat fluxes in the irrigated Gediz Basin, Turkey. J. Hydrol. 229 (1), 87–100.

Bastiaanssen, W.G.M., Menenti, M., Feddes, R.A., Holtslag, A.A.M., 1998a. A remote sensing surface energy balance algorithm for land (SEBAL). 1. Formulation. J. Hydrol. 212, 198–212.

Bastiaanssen, W.G.M., Pelgrum, H., Wang, J., Ma, Y., Moreno, J.F., Roerink, G.J., Van der Wal, T., 1998b. A remote sensing surface energy balance algorithm for land (SEBAL).: Part 2: validation. J. Hydrol. 212, 213–229.

Bastiaanssen, W.G.M., Noordman, E.J.M., Pelgrum, H., Davids, G., Thoreson, B.P., Allen, R.G., 2005. SEBAL model with remotely sensed data to improve water-resources management under actual field conditions. J. Irrigation Drainage Eng. 131 (1), 85–93.

Bastiaanssen, W.G.M., Cheema, M.J.M., Immerzeel, W.W., Miltenburg, I.J., Pelgrum, H., 2012. Surface energy balance and actual evapotranspiration of the transboundary Indus Basin estimated from satellite measurements and the ETLook model. Water Resour. Res. 48 (11).

Bausch, W.C., 1995. Remote sensing of crop coefficients for improving the irrigation scheduling of corn. Agric. Water Manage. 27 (1), 55–68.

Boronina, A., Golubev, S., Balderer, W., 2005. Estimation of actual evapotranspiration from an alluvial aquifer of the Kouris catchment (Cyprus) using continuous streamflow records. Hydrol. Process. 19 (20), 4055–4068.

Chemin, Y., Honda, K., 2006. Spatiotemporal fusion of rice actual evapotranspiration with genetic algorithms and an agrohydrological model. Geosci. Remote Sens., IEEE Trans. 44 (11), 3462–3469.

Choi, M., Kustas, W.P., Anderson, M.C., Allen, R.G., Li, F., Kjaersgaard, J.H., 2009. An intercomparison of three remote sensing-based surface energy balance algorithms over a corn and soybean production region (Iowa, US) during SMACEX. Agric. For. Meteorol. 149 (12), 2082–2097.
Chowdhury, S., Al-Zahrani, M., 2015. Characterizing water resources and trends of sector wise water consumptions in Saudi Arabia. J. King Saud Univ.-Eng. Sci. 27 (1), 68–82.
Department of Statistics and Information, 2013. Statistical Yearbook. Editions 38-44. Ministry of Economy and Planning, Kingdom of Saudi Arabia.
Droogers, P., Immerzeel, W.W., Lorite, I.J., 2010. Estimating actual irrigation application by remotely sensed evapotranspiration observations. Agric. Water Manage. 97 (9), 1351–1359.
El Tahir, M.E.H., Wenzhong, W., Xu, C.Y., Youjing, Z., Singh, V.P., 2011. Comparison of methods for estimation of regional actual evapotranspiration in data scarce regions: Blue Nile region, eastern Sudan. J. Hydrol. Eng. 17 (4), 578–589.
Elhaddad, A., Garcia, L.A., Chávez, J.L., 2010. Using a surface energy balance model to calculate spatially distributed actual evapotranspiration. J. Irrigation Drainage Eng. 137 (1), 17–26.
Fu, P., Rich, P.M., 1999. Design and implementation of the solar analyst: an ArcView extension for modeling solar radiation at landscape scales. In: Proceedings of the Nineteenth Annual ESRI User Conference, pp. 1–31.
Hafeez, M., Khan, S., 2005. Remote sensing application for estimation of irrigation water consumption in liuyuankou irrigation system in China. In: Proceedings 16th Congress of the Modelling and Simulation Society of Australia and New Zealand, pp. 12–15.
Li, S., Zhao, W., 2010. Satellite-based actual evapotranspiration estimation in the middle reach of the Heihe River Basin using the SEBAL method. Hydrol. Process. 24 (23), 3337–3344.
Liang, S., 2000. Narrowband to broadband conversions of land surface albedo I: Algorithms. Remote Sens. Environ. 76 (2), 213–238.
Liang, S., 2003. A direct algorithm for estimating land surface broadband albedos from MODIS imagery. Geosci. Remote Sens., IEEE Trans. 41 (1), 136–145.
Liu, W., Hong, Y., Khan, S.I., Huang, M., Vieux, B., Caliskan, S., Grout, T., 2010. Actual evapotranspiration estimation for different land use and land cover in urban regions using Landsat 5 data. J. Appl. Remote Sens. 4 (1), 041873–041873.
Mahmoud, S.H., 2014. Delineation of potential sites for groundwater recharge using a GIS-based decision support system. Environ. Earth Sci. 72 (9), 3429–3442.
Mahmoud, S.H., Alazba, A.A., 2016. Surface energy balance algorithm for land-based consumption water use of different land uses-cover types in arid-semiarid regions. Water Sci. Technol.: Water Supply. http://dx.doi.org/10.2166/ws.2016.077.
Mahmoud, S.H., Alazba, A.A., Amin, M.T., 2014. Identification of potential sites for groundwater recharge using a GIS-based decision support system in Jazan region-Saudi Arabia. Water Resour. Manage. 28 (10), 3319–3340.
Menenti, M., 1984. Physical aspects and determination of evaporation in deserts applying remote sensing techniques. Report 10, Inst. Land Water Managm. Res. (IWC), Wageningen, Niederlande, p. 202.
Minacapilli, M.A.R.I.O., Agnese, C.A.R.M.E.L.O., Blanda, F.E.D.E.R.I.C.O., Cammalleri, C. A.R.M.E.L.O., Ciraolo, G.I.U.S.E.P.P.E., D'Urso, G., Iovino, M., Pumo, D., Provenzano, G., Rallo, G., 2009. Estimation of actual evapotranspiration of Mediterranean perennial crops by means of remote-sensing based surface energy balance models. Hydrol. Earth Syst. Sci. 13 (7), 1061–1074.
Monin, A.S., Obukhov, A., 1954. Basic laws of turbulent mixing in the surface layer of the atmosphere. Contrib. Geophys. Inst. Acad. Sci. USSR 151, 163–187.
Monteith, J.L., 1965. Evaporation and environment. Symp. Soc. Exp. Biol., vol. 19, p. 4, No. 205-23.
Morse, A., Tasumi, M., Allen, R.G., Kramber, W.J., 2000. Application of the SEBAL Methodology for Estimating Consumptive Use of Water and Streamflow Depletion in the Bear River Basin of Idaho Through Remote Sensing. Idaho Department of Water Resources–University of Idaho.
Parodi, G., 1993. An up-to-date inventory of remote sensing potentially in the energy balance equation approach for actual evapotranspiration mapping. Basic theory and Prospects Doctoral dissertation, M.sc. thesis. ITC, Enschede, The Netherlands.
Ramos, J.G., Kay, J.A., Cratchley, C.R., Casterad, M.A., Herrero, J., López, R., Martínez-Cob, A., Domínguez, R., 2006. Crop management in a district within the Ebro River Basin using remote sensing techniques to estimate and map irrigation volumes. WIT Trans. Ecol. Environ. 96, 365–377.
Reuter, H.I., Nelson, A., Jarvis, A., 2007. An evaluation of void-filling interpolation methods for SRTM data. Int. J. Geographical Inf. Sci. 21 (9), 983–1008.
Ruiz-Arias, J.A., Tovar-Pescador, J., Pozo-Vázquez, D., Alsamamra, H., 2009. A comparative analysis of DEM-based models to estimate the solar radiation in mountainous terrain. Int. J. Geographical Inf. Sci. 23 (8), 1049–1076.
Sánchez, J.M., Scavone, G., Caselles, V., Valor, E., Copertino, V.A., Telesca, V., 2008. Monitoring daily evapotranspiration at a regional scale from Landsat-TM and ETM+ data: application to the Basilicata region. J. Hydrol. 351 (1), 58–70.
Santos, C.A.C.D., Bezerra, B.G., Silva, B.B.D., Rao, T.V.R., 2010. Assessment of daily actual evapotranspiration with SEBAL and S-SEBI algorithms in cotton crop. Revista Brasileira de Meteorologia 25 (3), 383–392.
Senay, G.B., Budde, M., Verdin, J.P., Melesse, A.M., 2007. A coupled remote sensing and simplified surface energy balance approach to estimate actual evapotranspiration from irrigated fields. Sensors 7 (6), 979–1000.
Singh, R.K., Irmak, A., Irmak, S., Martin, D.L., 2008. Application of SEBAL model for mapping evapotranspiration and estimating surface energy fluxes in south-central Nebraska. J. Irrigation Drainage Eng. 134 (3), 273–285.
Sun, Z., Wei, B., Su, W., Shen, W., Wang, C., You, D., Liu, Z., 2011. Evapotranspiration estimation based on the SEBAL model in the Nansi Lake Wetland of China. Math. Comput. Modell. 54 (3), 1086–1092.
Teixeira, A.D.C., Bastiaanssen, W.G.M., Ahmad, M., Bos, M.G., 2009. Reviewing SEBAL input parameters for assessing evapotranspiration and water productivity for the Low-Middle Sao Francisco River basin, Brazil: Part A: calibration and validation. Agric. For. Meteorol. 149 (3), 462–476.
Timmermans, W.J., Kustas, W.P., Anderson, M.C., French, A.N., 2007. An intercomparison of the surface energy balance algorithm for land (SEBAL) and the two-source energy balance (TSEB) modeling schemes. Remote Sens. Environ. 108, 369–384.
Wang, J., Ma, Y., Menenti, M., Bastiaanssen, W.G.M., Mitsuta, Y., 1995. The scaling-up of processes in the heterogeneous landscape of HEIFE with the aid of satellite remote sensing. J. Meteorol. Soc. Jpn. 73 (6), 1234–1244.
Wang, K., Wang, P., Li, Z., Cribb, M., Sparrow, M., 2007. A simple method to estimate actual evapotranspiration from a combination of net radiation, vegetation index, and temperature. J. Geophys. Res.: Atmos. 112 (D15).
Wanner, W., Strahler, A.H., Hu, B., Lewis, P., Muller, J.P., Li, X., Schaaf, C.L., Barnsley, M.J., 1997. Global retrieval of bidirectional reflectance and albedo over land from EOS MODIS and MISR data: theory and algorithm. J. Geophys. Res.: Atmos. 102 (D14), 17143–17161.
Wu, X., Zhou, J., Wang, H., Li, Y., Zhong, B., 2015. Evaluation of irrigation water use efficiency using remote sensing in the middle reach of the Heihe river, in the semi-arid Northwestern China. Hydrol. Process. 29 (9), 2243–2257.
Zhou, L., Dickinson, R.E., Tian, Y., Zeng, X., Dai, Y., Yang, Z.L., Schaaf, C.B., Gao, F., Jin, Y., Strahler, A., Myneni, R.B., 2003. Comparison of seasonal and spatial variations of albedos from Moderate-Resolution Imaging Spectroradiometer (MODIS) and Common Land Model. J. Geophys. Res.: Atmos. 108 (D15).